Electrostatic potential shape of gate-defined quantum point contacts

M. Geier [1,*], J. Freudenfeld [2], J. T. Silva [2], V. Umansky [3], D. Reuter [4,†], A. D. Wieck [4], P. W. Brouwer [1], and S. Ludwig [2]

[1]*Dahlem Center for Complex Quantum Systems and Physics Department, Freie Universität Berlin, Arnimallee 14, 14195 Berlin, Germany*
[2]*Paul-Drude-Institut für Festkörperelektronik, Leibniz-Institut im Forschungsverbund Berlin e.V., Hausvogteiplatz 5-7, 10117 Berlin, Germany*
[3]*Weizmann Institute of Science, Rehovot 76100, Israel*
[4]*Angewandte Festkörperphysik, Ruhr-Universität Bochum, Universitätsstrasse 150, 44780 Bochum, Germany*

Quantum point contacts (QPCs) are fundamental building blocks of nanoelectronic circuits. For their emission dynamics as well as for interaction effects such as the 0.7 anomaly the details of the electrostatic potential are important, but the precise potential shapes are usually unknown. Here, we measure the one-dimensional subband spacings of various QPCs as a function of their conductance and compare our findings with models of lateral parabolic versus hard-wall confinement. We find that a gate-defined QPC near pinch-off is compatible with the parabolic saddle-point scenario. However, as the number of populated subbands is increased, Coulomb screening flattens the potential bottom and a description in terms of a finite hard-wall potential becomes more realistic.

I. INTRODUCTION

Given the importance of quantum point contacts (QPCs) as fundamental building blocks of nanoelectronic circuits and the vast amount of literature on them [1–5], surprisingly little is known about the shape of their electrostatic potential as a function of the gate voltages. However, knowledge of the precise confinement potential is crucial for understanding interaction effects in QPCs [6–9] as well as their carrier emission dynamics [10,11], which is central for optimizing a quantum electronic circuit. The lateral confinement defines the mode structure of the one-dimensional (1D) channel, while the longitudinal potential shape governs the coupling of the 1D modes into the surrounding two-dimensional electron system (2DES). Populating the 1D channel with electrons by increasing the voltage applied to the split gates enhances Coulomb screening inside the constriction. As a consequence, the lateral confinement potential undergoes a transition from an unscreened approximately parabolic shape near pinch-off towards a screened potential for many occupied 1D subbands. Such a transition had been theoretically predicted [12]. Here, we experimentally demonstrate it using transport spectroscopy at finite source-drain voltage.

Details of the confinement vary between individual devices produced by various layouts based on different methods, which include the field effect [2,3], etching [13] or oxidation [14] techniques, and more [15,16]. The manifestation of 1D conductance quantization, $G = N G_Q$ with $G_Q = 2e^2/h$ and $N = 1, 2, 3, \ldots$, at cryogenic temperatures is often seen as a quality feature of QPCs. An "optimally" designed QPC has several conductance steps that are approximately equidistant in gate voltage as the QPC is opened up, starting from

pinch-off at $G = 0$. It is tempting to interpret the presence of equidistant conductance steps [2,17–21] as a signature of a parabolic transverse confinement potential as introduced in Ref. [22], since such a potential has transverse modes at equally spaced energies. However, this interpretation is questionable, as the distance of the conductance steps as a function of the gate voltage is not one-to-one related to the energy spacing of the 1D modes [20,23].

We study QPCs of two designs, but both defined using gate voltages by means of the electric field effect. In agreement with previous publications [4,9,21,22], our findings are consistent with a parabolic confinement potential near the pinch-off point of the QPCs. However, as the conductance of a QPC is increased, more and more carriers populate the 1D subbands and thereby arrange themselves to partially screen the electric field induced by the applied gate voltages. The resulting effective potential is then a function of the position of all charges, which also includes the usually not well-known distribution of surface states and charged bulk defects. A precise theoretical description of this screening effect requires a 3D self-consistent calculation, solving the classical Poisson equations together with the quantum mechanical Schrödinger equations [12,24,25]. A self-consistent Poisson-Schrödinger calculation performed for a set of fictitious boundary conditions and for the case of a standard split-gate-defined QPC suggests a transition from a parabolic lateral confinement for $N = 1$ towards a truncated parabola and, eventually, a hard-wall confinement as N is increased [12]. To test this scenario we measure nonlinear response transport through our QPC from which we identify the energy spacings between its highest occupied 1D modes. We compare our results to the two extreme scenarios for the lateral electrostatic confinement: parabolic confinement, as, e.g., in Refs. [19], [20], [26], and [27], and a hard-wall confinement, as, e.g., in Refs. [28] and [29]. Our results are inconsistent with parabolic confinement for $N \geqslant 4$ but are consistent with a transition from a

---

*maxgeier@zedat.fu-berlin.de
†Present address: Department of Physics, Paderborn University, Warburger Straße 100, 33098 Paderborn, Germany

parabolic lateral confinement at $N = 1$ towards a hard-wall potential as the QPCs are opened up.

II. TRANSPORT SPECTROSCOPY OF QUANTUM POINT CONTACTS

Our QPCs are formed using the electric field effect in a 2D electron system embedded 107 nm beneath the surface of a (Al,Ga)As/GaAs heterostructure. The 2DES's Fermi energy and mobility measured at cryogenic temperatures are $E_F \simeq$ 10.9 meV and $\mu_e \simeq 2.6 \times 10^6$ cm^2/V s for QPC$_1$ and similar for QPC$_2$. We performed all measurements in a helium-3 evaporation cryostat at temperatures near $T = 250$ mK. In Figs. 1(a) and 1(d), we present scanning electron microscope images of the two QPC samples and sketches of the gate layouts. For QPC$_1$ shown in Fig. 1(a) we use a standard split-gate layout and define the 1D constriction of the 2DES by applying a negative voltage V_g to both gates, while the 2DES and a back gate approximately 500 μm below the surface are at ground potential. The resulting linear response pinch-off curve, $G(V_g)/G_Q$, is presented in Fig. 1(b). It features clear and, for $N < 6$, nearly equidistant steps of quantized conductance. To create the second QPC$_2$ [see Fig. 1(d)], we use a global top gate to globally deplete the 2DES. Only below a screen gate placed in between the top gate and the 2DES we induce a finite density of free electrons [30]. The screen gate shapes a narrow constriction, i.e., a QPC between 2D leads. Both the QPC conductance and the carrier density in the leads are controlled by the combination of the voltages V_t and V_s applied to the top gate and screen gate, respectively. We present example pinch-off curves $G(V_t)$ for fixed $V_s = 0.5$ V and $G(V_s)$ for constant $V_t = -3.4$ V in Fig. 1(e). Note that the screen gate voltage is restricted to $V_s \lesssim 0.5$ V as a larger V_s causes a leakage current from the gate into the 2DES (as expected for a Schottky barrier).

All our pinch-off curves feature smooth transitions between quantized conductance plateaus. They indicate that the potential varies slowly and smoothly in current direction, reminiscent of a parabolic potential profile in the longitudinal direction, which results in reflectionless contacts between constriction and leads.

Quantized conductance is a consequence of the energy quantization in a 1D channel caused by the lateral confinement of the constriction. To experimentally determine the energies of the 1D modes we need a known energy scale to compare with. For this reason we measure the differential conductance $g = dI/dV$ (e.g., using a lock-in amplifier) as a function of the source-drain voltage V along the pinch-off curves. In Figs. 1(c) and 1(f) we plot the differential transconductances dg/dV_g (dg/dV_t) for the two QPCs as a function of the gate voltage and the bias voltage V_{QPC} (defined below) dropping across the QPC. In these plots steps of the conductance $G(V_g, V_{QPC})$ [$G(V_t, V_{QPC})$] appear as lines of positive differential transconductance (white). Red lines are a guide for the eye, indicating resonances between the 1D modes and the chemical potentials of the source and drain leads. Along the Nth line of positive (negative) slope counted from the bottom of the plot, the Nth 1D subband bottom energy is equal to the chemical potential in the source (drain) lead, $\varepsilon_N = \mu_S$ ($\varepsilon_N = \mu_D$). The lines frame diamond-shaped regions

around $V_{QPC} = 0$. Within these regions the conductance takes the quantized values $G = NG_Q$. Intersection points at $V_{QPC} = 0$ indicate steps of the linear response pinch-off curves, i.e., $G = (N - 0.5)G_Q$. At intersection points at finite $V_{QPC} \neq 0$ the chemical potential drop across a QPC equals the energy spacing between the corresponding 1D modes, $|\mu_S - \mu_D| = eV_{QPC} = \varepsilon_N - \varepsilon_M$. The additional curved lines of enhanced differential transconductance within the $N = 1$ diamond indicate the 0.7 anomaly [5–9], which is not a topic of this article.

Since the source-drain voltage V is applied across the QPC *and its leads* (which is always the case, because of the finite contact sizes even for a four-terminal measurement), the voltage drop across a QPC is $V_{QPC} = V - V_{lead} = V - R_{lead}I$ [cf. sketch in Fig. 1(b)]. The lead resistance can be directly determined from the linear response pinch-off curves by forcing the conductance plateaus to their quantized values, $R_{lead} = V/I - (NG_Q)^{-1}$. Our pinch-off curves in Figs. 1(b) and 1(e) are already corrected for the lead resistances, while for QPC$_1$ we additionally plot the uncorrected curve, i.e., the raw data, as a solid line. For completeness we present the lead resistances for all three pinch-off curves in Fig. 2.

From these we determine the voltage drop across the QPC, $V_{QPC} = V/(R_{lead}G + 1)$, which is the x axis in Figs. 1(c) and 1(f). The tapered shape of the region of plotted data is a result of correcting for the lead resistances (we measured between -8 mV $\leqslant V \leqslant 8$ mV).

At the intersection points marked by red squares in Figs. 1(c) and 1(f) the bias V_{QPC} is precisely equal to the energy spacings between subsequent subbands,

$$\delta\varepsilon(N) = \varepsilon_{N+1} - \varepsilon_N = eV_{QPC}. \tag{1}$$

We plot $\delta\varepsilon(N)$ in Fig. 3 for all three pinch-off curves. Related to the variations in geometry the three implementations of QPCs have different subband spacings. However, as a general feature we observe a strong decrease in $\delta\varepsilon(N)$ as the QPCs are opened and N is increased.

III. HARD-WALL VERSUS PARABOLIC LATERAL CONFINEMENT

Given reflectionless contacts, the conductance of a QPC is limited by its strongest lateral confinement in the center of the constriction. The measured subband spacings are uniquely related with this lateral confinement. In the following, we compare the two most common models describing the lateral confinement, namely, a hard-wall versus a parabolic potential. These two models may be considered the extreme limits of a "continuum" of realistic scenarios for the transverse confinement.

A. Lateral hard-wall potential

For the lateral hard-wall potential we model the transverse confinement potential $\Phi(y)$ as

$$\Phi(y) = \begin{cases} \Phi_0, & |y| \leqslant W/2, \\ \infty, & |y| > W/2, \end{cases} \tag{2}$$

where the two parameters W and Φ_0 are the width and offset of the hard-wall potential well. An offset can be caused by a partial depletion of the constriction related to the incomplete
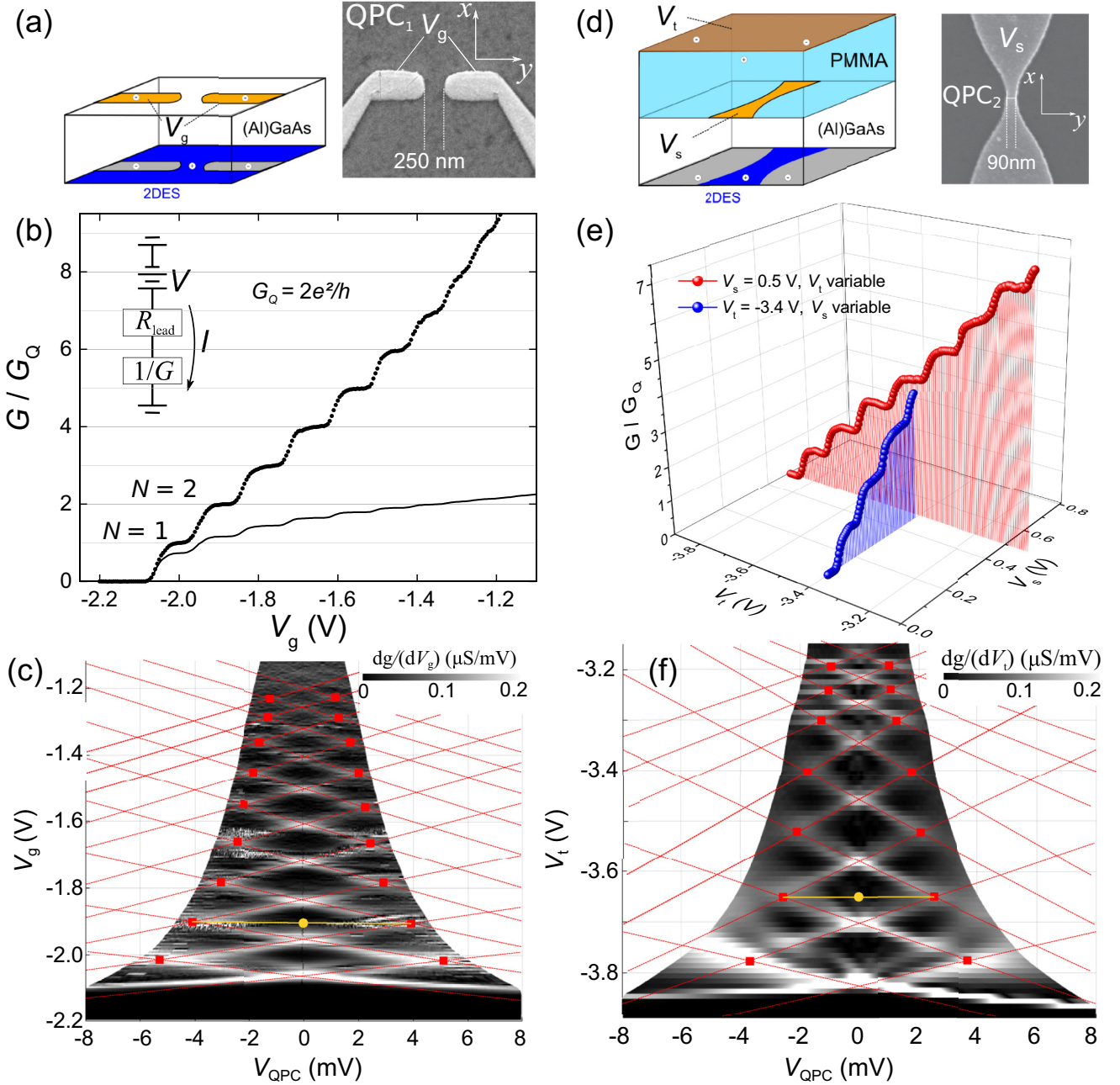
FIG. 1. (a) Scanning electron microscope (SEM) picture of Ti/Au gates (light-gray regions) on the wafer surface (dark region) of QPC_1 and sketch of the electric field effect device. Negative voltage V_g applied to the gates (yellow regions) is used to locally deplete the 2DES (blue where conducting, gray where depleted) 107 nm beneath the surface. (b) Pinch-off curve $G(V_g)/G_Q$ of QPC_1 using the source-drain voltage $V = -0.5$ mV. Solid line, raw data; dotted line, corrected for lead resistance $R_{lead} = 4.62$ kΩ, which includes 4.4 kΩ resistance of external RC filters. Inset: Simplified circuit diagram of the measurement. (c) Finite-bias spectroscopy of QPC_1, $dg/dV_g(V_{QPC}, V_g)$, accounting for the lead resistance (see the text). Local maxima of dg/dV_g (white lines) indicate transitions between adjacent conductance plateaus. (d) SEM picture of a screen gate equivalent to that of QPC_2. As shown in the sketch, the actual device is covered with a 130-nm-thick layer of cross-linked PMMA which carries a global top gate. (e) Pinch-off curves of QPC_2 corrected for a gate-voltage-dependent lead resistance, including a constant 4.4-kΩ resistance of external RC filters (cf. Fig. 2): $G(V_t)/G_Q$ for $V_s = 0.5$ V and $G(V_s)/G_Q$ for $V_t = -3.4$ V at $V = -0.1$ mV. (f) $dg/dV_g(V_{QPC}, V_t)$ of QPC_2, accounting for the lead resistance. Additional lines and symbols in (c) and (f) are explained in the text.

screening in a semiconductor with a low carrier density. The threshold energies for the transverse modes are

$$E_n = \frac{\pi^2 \hbar^2 n^2}{2m^\star W^2} + \Phi_0, \qquad (3)$$

where $m^\star = 0.067 m_0$ is the effective mass of the electrons in GaAs, m_0 being the free electron mass. Using Eq. (1) to relate the bias voltage at the intersection points marked by the red squares in Figs. 1(c) and 1(f) to the subband spacing $\delta\varepsilon(N) =$
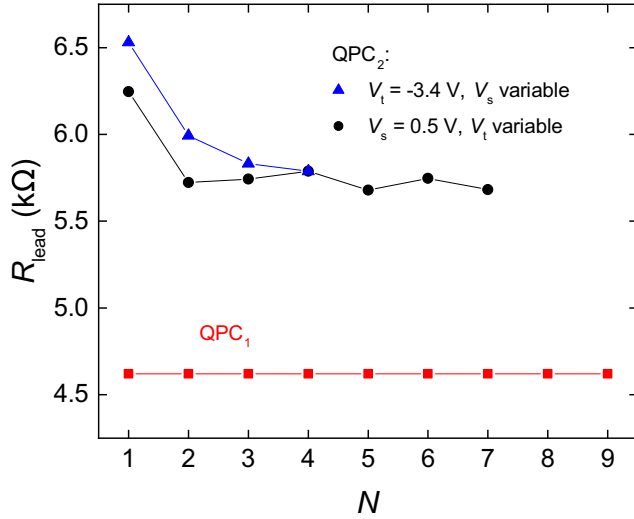
FIG. 2. Resistances R_{lead} of the leads to the QPCs [cf. sketch in Fig. 1(b)]. For the split-gate design of QPC$_1$ R_{lead} is constant, while it is a function of gate voltages for QPC$_2$.

$E_{N+1} - E_N$, we calculate the widths

$$W(N) = \pi \hbar \sqrt{\frac{2N+1}{2m\delta\varepsilon(N)}}. \tag{4}$$

Neglecting additional screening effects from the applied bias voltage, these values of $W(N)$ apply everywhere along the (almost-horizontal) lines connecting pairs of red squares [see the yellow lines for $N = 2$ in Figs. 1(c) and 1(f)]. In particular, this allows us to extend our estimate of the width $W(N)$ to $V_{\text{QPC}} = 0$, indicated for $N = 2$ by the small yellow circle in Figs. 1(c) and 1(f). Substituting W in Eq. (3) with $W(N)$,
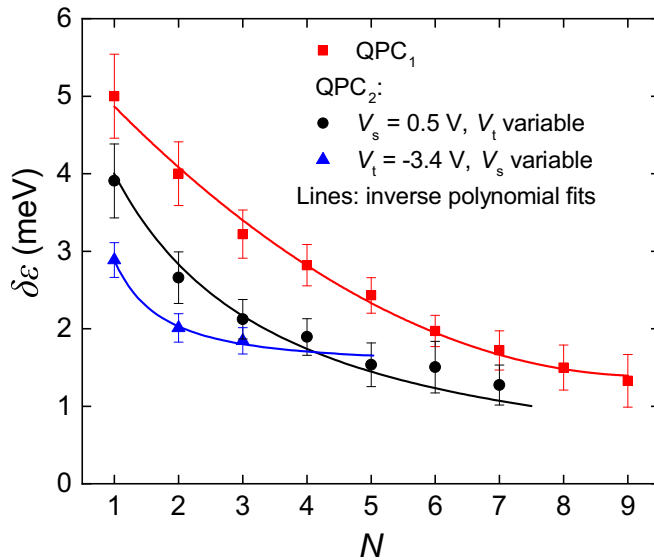

FIG. 3. Subband spacings $\delta\epsilon(N)$ of both QPCs for the three pinch-off curves presented in Fig. 1. Lines are guides for the eyes. At the intersection of the two lines of QPC$_2$ the gate voltages V_s and V_t will be identical for both measurements. Error bars reflect the uncertainties of the red lines in Figs. 1(c) and 1(d).

we then find the potential offset Φ_0 using the relation $E_{\text{F}} \simeq E_N + 0.5\delta\epsilon(N)$, which gives

$$\Phi_0(N) \simeq E_{\text{F}} - \delta\varepsilon(N) \left(\frac{N^2}{2N+1} + \frac{1}{2} \right). \tag{5}$$

The potential shift by $0.5\delta\epsilon(N)$ accounts for the difference between the Nth subband bottom E_N and the Fermi level E_{F} in the center of each diamond at $V_{\text{QPC}} = 0$, assuming symmetric coupling between the 1D constriction and both leads. [The assumption of symmetric coupling is confirmed by the fact that the lines connecting pairs of red squares in Figs. 1(c) and 1(f) are almost horizontal.]

B. Lateral parabolic potential

To model a lateral parabolic potential we use

$$\Phi(y) = \Phi_0 + \frac{m\omega_y^2 y^2}{2}, \tag{6}$$

where ω_y and Φ_0 are the characteristic frequency and offset of the parabolic potential well. In analogy to the analysis assuming hard-wall potentials, we determine the two parameters from the measured subband spacings. At the intersection points indicated by red squares in Figs. 1(c) and 1(f), we find

$$\hbar\omega_y(N) = eV_{\text{QPC}} = \delta\varepsilon(N), \tag{7}$$

and in the centers of the diamonds at $V_{\text{QPC}} = 0$, in addition,

$$\Phi_0(N) \simeq E_{\text{F}} - N\hbar\omega_y. \tag{8}$$

C. Comparison of the two potential shapes

We directly compare our results for the hard-wall potential shown in Figs. 4(a)–4(c) and for the assumption of parabolic confinement plotted in Figs. 4(d)–4(f). We present the parameters W and Φ_0 as a function of the subband number N for all three QPC implementations for the hard-wall potential in Figs. 4(a) and 4(b) and ω_y and Φ_0 for the parabolic potential in Figs. 4(d) and 4(e). The results are qualitatively similar for the various implementations of QPCs; the variations in W or ω_y between QPCs indicate that the lateral confinement potential of QPC$_2$ is slightly wider compared to that of QPC$_1$. In Figs. 4(c) and 4(f), showing the actual potentials for QPC$_1$, for comparison we indicate the lithographic distance of 250 nm between the gates shown in the inset in Fig. 1(a). It corresponds to the white area between regions of gray background. The width of the hard-wall potential slightly exceeds the lithographic width for $N = 9$. QPC$_1$ does not show further plateaus for $N > 9$.

Comparing the two models a substantial difference is visible in $\Phi_0(N)$. While for $N = 1$ the potential offset is similar for both models with $\Phi_0/E_{\text{F}} \simeq 0.6$, in the case of the hard-wall potential it slowly decreases to $\Phi_0/E_{\text{F}} \simeq 0.4$ at $N = 4$ and stays approximately constant at that level as the QPC is opened further. In contrast, the decrease in the offset $\Phi_0(N)$ of the parabolic potential with N is much steeper, such that for $N \gtrsim 4$ it moves below the bottom of the conduction band in the 2D leads, indicated as the dashed line at $\Phi = 0$. We are not aware of a realistic mechanism that could lead to such an overscreening of the negative voltages applied to the control gates (V_g for QPC$_1$ or V_t for QPC$_2$).
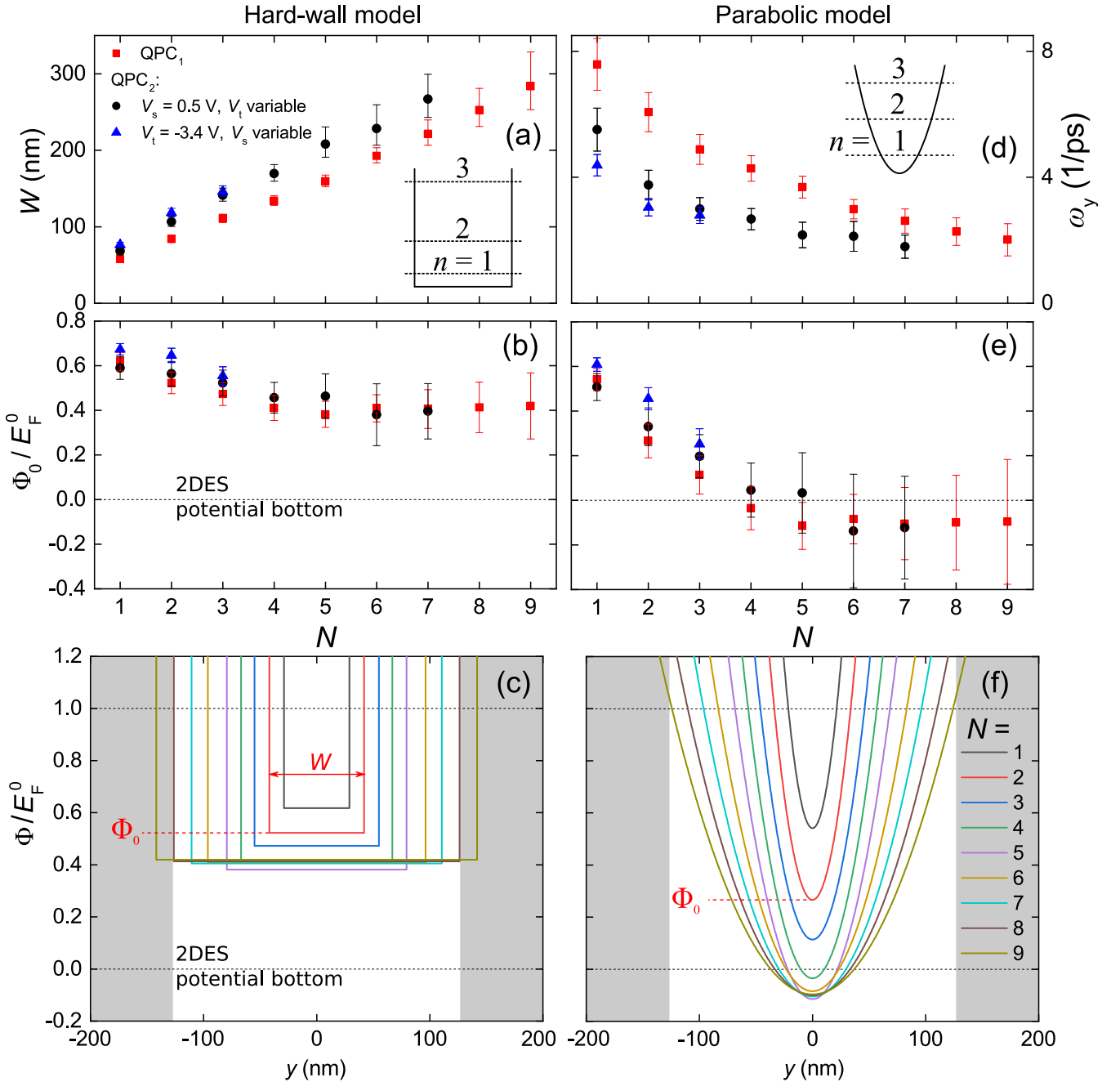
FIG. 4. Comparison between hard-wall (a–c) and parabolic (d–f) potential models of the lateral confinement. (a) Width of the hard-wall potential $W(N)$. (b) Offset of the hard-wall potential $\Phi_0(N)$. (c) Shape of the hard-wall potential for $1 \leqslant N \leqslant 9$, only for QPC_1. (d) Curvature of the parabolic potential $\omega_y(N)$. (e) Offset of the parabolic potential $\Phi_0(N)$. (f) Shape of the parabolic potential for $1 \leqslant N \leqslant 9$, only for QPC_1. Error bars in (a), (b), (d), and (e) are calculated by error propagation from the error of $\delta\varepsilon(N)$ (cf. Fig. 3).

IV. DISCUSSION AND SUMMARY

The main result of our simple analysis starting from the measured subband spacings $\delta\varepsilon(N)$ is that for $N \geqslant 4$ we can exclude a parabolic lateral confinement potential for our QPCs. Based on a self-consistent calculation it has been suggested that the increasing population of the 1D constriction with N as a QPC is opened up leads to an increased screening of the electric field originating from the charged control gates. For a gate-defined QPC, this process can cause a transition from a parabolic confinement for the case of little screening,

i.e., $N = 1$ towards a truncated potential with a flat bottom at larger N where many carriers populate the constriction [12]. Our findings support such a scenario. The hard-wall potential presents a somewhat unrealistic extreme case of strong screening. Nevertheless, for $N \geqslant 4$ it seems more realistic than the other extreme, namely the parabolic potential. The true shape of the lateral confinement potential of a QPC for $N \geqslant 4$ likely lies between these two extremes, maybe close to a truncated parabola [12,31], i.e., a parabola with a flat bottom identical to that of a hard-wall potential but with smoothly increasing side walls of constant curvature as the case for a parabola.

In summary, a parabolic saddle-point potential is likely a realistic description of a QPC near pinch-off, although our measurement can also be explained with a hard-wall confinement in this regime. However, as the QPC is opened up beyond $N \simeq 4$, the parabolic lateral confinement turns out to be a bad approximation. In this regime of enhanced screening, a hard-wall potential is the better approximation.

APPENDIX

1. Coupling between control gates and the QPC

The electrostatic potential shaping the QPCs is generated and controlled via the field effect by applying voltages to nearby metal gates. The size of the plateaus of quantized conductance in the pinch-off curves as a function of the gate voltage [cf. Figs. 1(b) and 1(e)] is proportional to the capacitive coupling between the control gates and the QPC, which we approximate as a conducting 1D channel with the carrier density n_{1D}. We determine the approximate capacitance per unit length between gate and QPC as

$$c_{1D} = e\delta n_{1D}/\delta V_{gate}, \quad (A1)$$

where δn_{1D} is the carrier density increase as the voltage on the control gate is increased by δV_{gate}. If we take for δV_{gate} the voltage difference between two subsequent intersection points of the source and drain resonances at $V_{QPC} = 0$ in Figs. 1(c) and 1(f), δn_{1D} corresponds to the difference in the values of n_{1D} at these points with N versus $N + 1$ subbands being populated. The 1D carrier density is

$$n_{1D}(N) = \int_0^\infty D_{1D}(E)f(E)\mathrm{d}E, \quad (A2)$$

where $D_{1D} = \frac{1}{\pi\hbar}\sqrt{\frac{2m^\star}{E}}$ is the 1D electron density of states and $f(E)$ the Fermi-Dirac distribution. Given $k_B T \ll E_F$, we approximate $f(E) = 1$ for $E < E_F$ and $f(E) = 0$ for $E > E_F$. Summing up all 1D modes which are actually populated for the QPC tuned to the conductance $G = NG_Q$, we find

$$n_{1D}(N) = \frac{\sqrt{2m^\star}}{\pi\hbar} \sum_{n=1}^N \int_{E_n}^{E_F} \frac{1}{\sqrt{E - E_n}} dE$$

$$= \frac{\sqrt{8m^\star}}{\pi\hbar} \sum_{n=1}^N \sqrt{E_F - E_n}. \quad (A3)$$

Inserting $\delta n_{1D}(N) = n_{1D}(N + 1) - n_{1D}(N)$ from Eq. (11) into Eq. (A1), we finally determine the 1D capacitance density as

$$c_{1D}(N) = \frac{\sqrt{8m^\star e^2}}{\pi\hbar} \frac{\sqrt{E_F - E_{N+1}}}{\delta V_{gate}(N)}, \quad (A4)$$
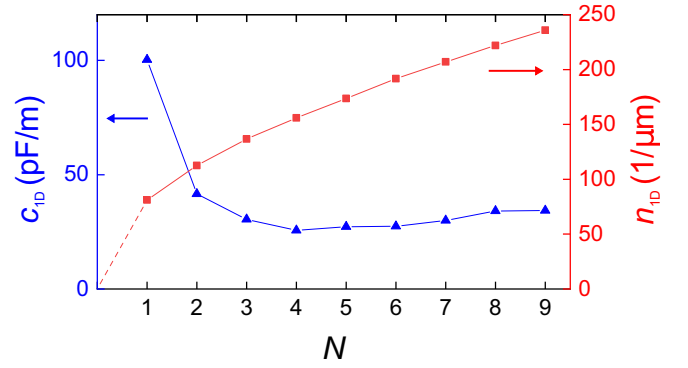

FIG. 5. One-dimensional carrier density $n_{1D}(N)$, assuming an infinitely long hard-wall 1D channel of width $W(N)$ and depth $E_F - \Phi_0(N)$ of QPC$_1$ (red squares; right-side axis) and the corresponding 1D capacitance density $c_{1D}(N)$ (blue triangles; left-side axis).

where $\delta V_{gate}(N)$ is the width of the Nth plateau of the pinch-off curve (cf. Fig. 1) measured between the conductances $(N + 0.5)G_Q$ and $(N - 0.5)G_Q$. Substituting E_{N+1} with the according eigenenergy of the hard-wall potential using Eq. (3), we can now determine $c_{1D}(N)$. In Fig. 5, we present the 1D capacitance density $c_{1D}(N)$, which is the slope of the also shown 1D carrier density $n_{1D}(N)$. The strong decrease in the capacitance with N for $N \leqslant 4$ is a direct signature of the increase in the screening of the electric field of the gates with a growing carrier density.

In addition, the variations in capacitance as a function of N explain the counterintuitive result that the subband spacings $\delta\epsilon(N)$ strongly vary in a region of almost-equal widths of the plateaus of quantized conductance of the pinch-off curve [cf. Figs. 1(b) and 1(e) and Fig. 3].

2. Width of the 1D constriction as a function of the gate voltage

In Fig. 4(a), we present the width of the hard-wall potential $W(N)$. In Fig. 6, we plot $W(V_g)$ for QPC$_1$. Next, we compare this result with the dependence of the depletion region of a gate voltage using a different sample on the same wafer
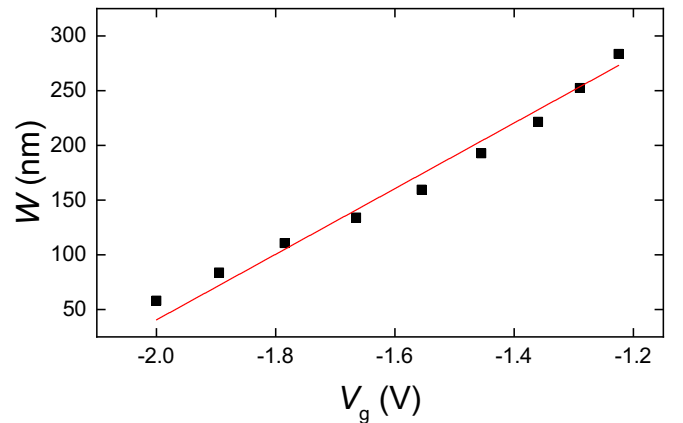

FIG. 6. Width of the hard-wall potential $W(V_g)$ for QPC$_1$ [same data as the $W(N)$ in Fig. 4(a)]. The slope of the red line is $\mathrm{d}W/\mathrm{d}V_g = 300$ nm/V (cf. the text).
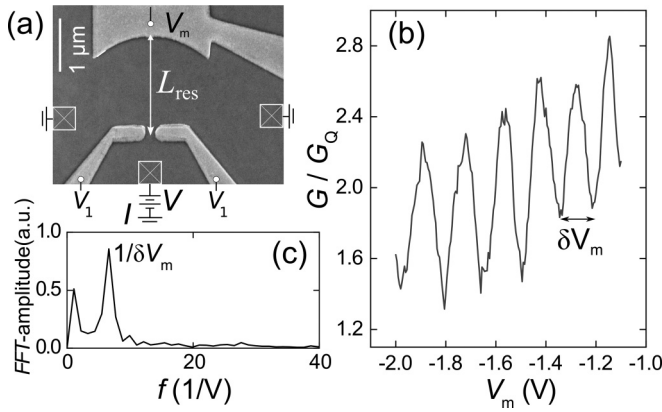
FIG. 7. (a) QPC nominally identical to QPC$_1$ for $N = 4$, coupled to a hemispherical mirror which is defined by a negative gate voltage V_m. (b) Conductance of the QPC as a function of V_m. (c) Fourier transform of the conductance. From the peak value, we determine the period $\delta V_m \simeq 150$ mV of the oscillations in (b).

material. The sample shown in Fig. 7(a) contains a QPC nominally identical to QPC$_1$ and a hemispherical mirror gate. The two samples have been prepared in parallel and on the same wafer. In Fig. 7(b) we present the conductance of the QPC as a function of the voltage applied to the mirror gate. The bare conductance (without mirror) is $G = 4G_Q$. However, with the 2DES below the mirror gate depleted it is reduced by roughly a factor of 2, because of enhanced backscattering through the QPC. At the same time, $G(V_m)$ oscillates with a visibility of 40%. Both the conductance reduction and the

oscillation are related to the formation of localized modes inside the hemispherical resonator. The oscillation can be interpreted in analogy to the oscillations of the standing wave in a Fabry-Pérot resonator, while here, the coherent electrons generate the standing wave. By increasing the gate voltage V_m, we decrease the area of 2DES depleted next to the mirror gate and thereby increase the length of the resonator (the distance between the QPC and the mirror). Per period of the conductance oscillation, the length of the resonator is reduced by half of the Fermi wavelength $dL_{res}/dV_m = 0.5\lambda_F/\delta V_m$ with the resonator length L_{res}. We determine the averaged period from the fast Fourier transform of the oscillation [cf. Fig. 7(c)] and find $\delta V_m \simeq 150$ mV. With $\lambda_F = 45$ nm, we finally estimate the rate of the depletion length reduction as $dL_{res}/dV_m = 150$ nm/V. Changing the voltage applied to the QPC gates instead of the mirror gates results in the same conclusion, while in this case the interference pattern appears on top of the QPC pinch-off curve.

To estimate the depletion of the electron system between the QPC gates, we have to add up the electric fields of both gates. Based on the fact that the same voltage is applied to both gates and the distance between gates is more than two times larger than the distance between each gate and the 2DES, we neglect any influences that a gate has on the depletion caused by the other gate. From the slope of the red line in Fig. 6 we find the dependence of the width of the hard-wall potential $W(V_g)$ as a function of the gate voltage to be $dW/dV_g \simeq 300$ nm/V, twice as large as the effect of a single-mirror gate. This finding supports the applicability of the hard-wall model for QPCs with $N \geqslant 4$.

[1] R. Landauer, Phys. Lett. A **85**, 91 (1981).

[2] B. J. van Wees, H. van Houten, C. W. J. Beenakker, J. G. Williamson, L. P. Kouwenhoven, D. van der Marel, and C. T. Foxon, Phys. Rev. Lett. **60**, 848 (1988).

[3] D. A. Wharam, T. J. Thornton, R. Newbury, M. Pepper, H. Ahmed, J. E. F. Frost, D. G. Hasko, D. C. Peacock, D. A. Ritchie, and G. A. C. Jones, J. Phys. C: Solid State Phys. **21**, L209 (1988).

[4] K.-F. Berggren and M. Pepper, Philos. Trans. R. Soc. A **368**, 1141 (2010).

[5] A. P. Micolich, J. Phys.: Condens. Matter **23**, 443201 (2011).

[6] T. Rejec and Y. Meir, Nature **442**, 900 (2006).

[7] E. J. Koop, A. I. Lerescu, J. Liu, B. J. van Wees, D. Reuter, A. D. Wieck, and C. H. van der Wal, J. Supercond. Novel Magn. **20**, 433 (2007).

[8] F. Bauer, J. Heyder, E. Schubert, D. Borowsky, D. Taubert, B. Bruognolo, D. Schuh, W. Wegscheider, J. von Delft, and S. Ludwig, Nature **501**, 73 (2013).

[9] J. Heyder, F. Bauer, E. Schubert, D. Borowsky, D. Schuh, W. Wegscheider, J. von Delft, and S. Ludwig, Phys. Rev. B **92**, 195401 (2015).

[10] M. A. Topinka, B. J. LeRoy, S. E. J. Shaw, E. J. Heller, R. M. Westervelt, K. D. Maranowski, and A. C. Gossard, Science **289**, 2323 (2000).

[11] J. Freudenfeld, M. Geier, V. Umansky, P. Brouwer, and S. Ludwig, arXiv:2002.12340.

[12] S. Laux, D. Frank, and F. Stern, Surface Sci. **196**, 101 (1988).

[13] T. P. Martin, C. A. Marlow, L. Samuelson, A. R. Hamilton, H. Linke, and R. P. Taylor, Phys. Rev. B **77**, 155309 (2008).

[14] V. Senz, T. Heinzel, T. Ihn, S. Lindemann, R. Held, K. Ensslin, W. Wegscheider, and M. Bichler, J. Phys.: Condens. Matter **13**, 3831 (2001).

[15] C. Fricke, J. Regul, F. Hohls, D. Reuter, A. Wieck, and R. Haug, Physica E: Low-Dimension. Syst. Nanostruct. **34**, 519 (2006).

[16] C. Rössler, M. Herz, M. Bichler, and S. Ludwig, Solid State Commun. **150**, 861 (2010).

[17] R. Taboryski, A. Kristensen, C. B. Sørensen, and P. E. Lindelof, Phys. Rev. B **51**, 2282 (1995).

[18] K. J. Thomas, J. T. Nicholls, N. J. Appleyard, M. Y. Simmons, M. Pepper, D. R. Mace, W. R. Tribe, and D. A. Ritchie, Phys. Rev. B **58**, 4846 (1998).

[19] W. Hew, K. Thomas, I. Farrer, D. Anderson, D. Ritchie, and M. Pepper, Physica E: Low-Dimension. Syst. Nanostruct. **40**, 1645 (2008).

[20] C. Rössler, S. Baer, E. de Wiljes, P.-L. Ardelt, T. Ihn, K. Ensslin, C. Reichl, and W. Wegscheider, New J. Phys. **13**, 113006 (2011).

[21] A. M. Burke, O. Klochan, I. Farrer, D. A. Ritchie, A. R. Hamilton, and A. P. Micolich, Nano Lett. **12**, 4495 (2012).

[22] M. Büttiker, Phys. Rev. B **41**, 7906 (1990).

[23] A. P. Micolich and U. Zülicke, J. Phys.: Condens. Matter **23**, 362201 (2011).

[24] I. I. Yakimenko, V. S. Tsykunov, and K.-F. Berggren, J. Phys.: Condens. Matter **25**, 072201 (2013).

[25] S. Birner, T. Zibold, T. Andlauer, T. Kubis, M. Sabathil, A. Trellakis, and P. Vogl, IEEE Trans. Electron Devices **54**, 2137 (2007).

[26] J. F. Weisz and K.-F. Berggren, Phys. Rev. B **40**, 1325 (1989).

[27] J. Song, Y. Kawano, K. Ishibashi, J. Mikalopas, G. R. Aizin, N. Aoki, J. L. Reno, Y. Ochiai, and J. P. Bird, Appl. Phys. Lett. **95**, 233115 (2009).

[28] B. J. van Wees, L. P. Kouwenhoven, H. van Houten, C. W. J. Beenakker, J. E. Mooij, C. T. Foxon, and J. J. Harris, Phys. Rev. B **38**, 3625 (1988).

[29] K. Gloos, P. Utko, M. Aagesen, C. B. Sørensen, J. B. Hansen, and P. E. Lindelof, Phys. Rev. B **73**, 125326 (2006).

[30] N. Bachsoliani, S. Platonov, A. D. Wieck, and S. Ludwig, Phys. Rev. Appl. **8**, 064015 (2017).

[31] D. A. Wharam, U. Ekenberg, M. Pepper, D. G. Hasko, H. Ahmed, J. E. F. Frost, D. A. Ritchie, D. C. Peacock, and G. A. C. Jones, Phys. Rev. B **39**, 6283 (1989).